Title

Charge-State Control of Mn(2+) Spin Relaxation Dynamics in Colloidal n-Type Zn1-xMnxO Nanocrystals.

Journal

The journal of physical chemistry letters, 6(9)

ISSN

1948-7185

Authors

Schimpf, Alina M
Rinehart, Jeffrey D
Ochsenbein, Stefan T
et al.

Publication Date

2015-05-01

DOI

10.1021/acs.jpclett.5b00621

Peer reviewed

THE JOURNAL OF PHYSICAL CHEMISTRY Letters

Letter

pubs.acs.org/JPCL

Charge-State Control of Mn^{2+} Spin Relaxation Dynamics in Colloidal *n*-Type $Zn_{1-x}Mn_xO$ Nanocrystals

Alina M. Schimpf, Jeffrey D. Rinehart,[†] Stefan T. Ochsenbein,[‡] and Daniel R. Gamelin*

Department of Chemistry, University of Washington, Seattle, Washington 98195-1700, United States

Supporting Information

ABSTRACT: Colloidal diluted magnetic semiconductor (DMS) nanocrystals are model systems for studying spin effects in semiconductor nanostructures with relevance to future spin-based information processing technologies. The introduction of excess delocalized charge carriers into such nanocrystals turns on strong dopant−carrier magnetic exchange interactions, with important consequences for the physical properties of these materials. Here, we use pulsed electron paramagnetic resonance (pEPR) spectroscopy to probe the effects of excess conduction band electrons on the spin dynamics of colloidal Mn^{2+}-doped ZnO nanocrystals. Mn^{2+} spin−lattice relaxation is strongly accelerated by the addition of even one conduction band electron per $Zn_{1-x}Mn_xO$ nanocrystal, attributable to the introduction of a new exchange-based Mn^{2+} spin relaxation pathway. A kinetic model is used to describe the enhanced relaxation rates, yielding new insights into the spin dynamics and electronic structures of these materials with potential ramifications for future applications of DMS nanostructures in spin-based technologies.

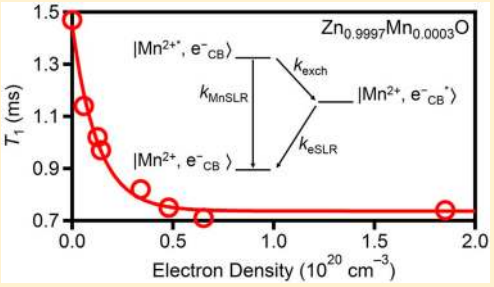

Diluted magnetic semiconductor (DMS) nanostructures are attractive targets for emerging spintronic and quantum computing applications[1−4] due to their large carrier−dopant magnetic exchange interactions[5−7] and the ability to electronically and optically manipulate or read out the magnetic dopant spins.[8,9] One particular motif that has received broad attention involves the incorporation of Mn^{2+} cations into colloidal semiconductor nanocrystals. Substitutional Mn^{2+} doping of colloidal semiconductor nanocrystals has been demonstrated, with compositions ranging from many hundreds of Mn^{2+} cations per nanocrystal down to a single Mn^{2+} per nanocrystal.[10] An interesting feature of colloidal nanocrystals is that many such systems can be photochemically reduced to introduce a well-defined number of stable, delocalized band-like electrons.[11−13] In Mn^{2+}-doped nanocrystals, this chemistry turns on new exchange interactions between the delocalized electrons and the $S = 5/2$ Mn^{2+} dopant ions, allowing the impact of delocalized carriers on nanocrystal physical properties to be examined systematically.[14]

Previous studies have demonstrated that Mn^{2+}−Mn^{2+} exchange interactions and spin polarizations can be effectively manipulated in colloidal nanocrystals via the introduction and removal of excess electrons[14] or excitons.[15] Less is known, however, about the effects of excess free carriers on the dynamics of dopant spins in colloidal DMS nanocrystals. Such dynamics will eventually govern many device-relevant characteristics, from polarization switching frequencies to the available time scales for coherent operations. Quantitative understanding of the effects of proximate electrons or holes on spin−lattice relaxation and quantum coherence times of magnetic dopants is thus vital to developing technologies based on DMS nanocrystal architectures. Here, we use a combination of nanocrystal photodoping and electron paramagnetic resonance (EPR) spectroscopy to demonstrate charge-tunable spin relaxation dynamics of Mn^{2+} dopants in colloidal ZnO nanocrystals.

Three samples were examined, $d = 3.7$ nm $Zn_{0.9997}Mn_{0.0003}O$, $d = 3.7$ nm $Zn_{0.996}Mn_{0.004}O$, and $d = 7.8$ nm $Zn_{0.997}Mn_{0.003}O$ nanocrystals, with the focus primarily on the first two. Figure 1a shows the room-temperature continuous wave (CW) EPR spectrum of colloidal $d = 3.7$ nm $Zn_{0.996}Mn_{0.004}O$ nanocrystals. The rich Mn^{2+} hyperfine structure is similar to that observed in bulk $Zn_{1-x}Mn_xO$, indicative of substitutional doping.[16] Excess delocalized electrons were added to the conduction bands of these $Zn_{1-x}Mn_xO$ nanocrystals via photochemical reduction (see the Methods section).[11−14,17,18] These electrons fill the nanocrystal volume and do not localize even at cryogenic temperatures.[14,17,19,20] The CW EPR spectrum of fully reduced nanocrystals is shown in Figure 1a (blue). Introduction of conduction band electrons leads to a substantial broadening of the Mn^{2+} EPR signal and an increase in its total integrated intensity (Figure 1b).[11,14] The increased resonance intensity has been analyzed in detail previously and was shown to arise from new Mn^{2+}−Mn^{2+} magnetic exchange interactions that are activated by the excess conduction band electrons.[14]

The broadening of the Mn^{2+} CW EPR spectrum upon photodoping suggests increased spin−spin and/or spin−lattice relaxation rates. To investigate the effect of conduction band electrons on Mn^{2+} spin relaxation times, pulsed EPR measurements were conducted at 4.5 K. Figure 2a shows electron spin-

Received: March 24, 2015
Accepted: April 20, 2015
Published: April 20, 2015

DOI: 10.1021/acs.jpclett.5b00621
J. Phys. Chem. Lett. 2015, 6, 1748−1753

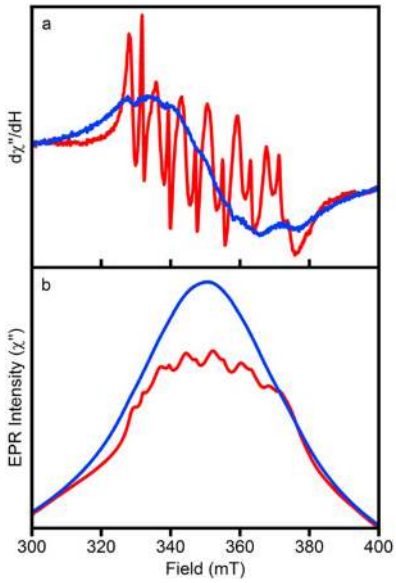

Figure 1. Room-temperature X-band CW EPR spectra of as-prepared (red) and maximally reduced (blue) colloidal d = 3.7 nm $Zn_{0.996}Mn_{0.004}O$ nanocrystals, plotted in (a) derivative and (b) absorptive mode.

echo (ESE) spectra of the as-prepared d = 3.7 nm $Zn_{0.9997}Mn_{0.0003}O$ nanocrystals (red) and of the same nanocrystals after maximum photochemical reduction (blue). CW EPR spectra are provided in Figure S1 (Supporting Information). A slight broadening of the signal and a decrease in overall intensity is observed upon photodoping. The sharp signal at ∼360 mT is due to conduction band electrons in undoped ZnO nanocrystals that are present in the ensemble at these very low Mn^{2+} concentrations. For d = 3.7 nm $Zn_{0.9997}Mn_{0.0003}O$ nanocrystals, there is an average of 0.33 Mn^{2+} per nanocrystal, meaning ∼2/3 of the nanocrystals contain no Mn^{2+}.

To quantify spin−lattice relaxation times (T_1), the echo intensity was measured as a function of delay time (τ) using an echo-detected inversion recovery sequence ($\pi - \tau - \pi/2 - T_{fixed} - \pi - T_{fixed}$ − echo). These decays are shown in Figure 2b for the same nanocrystals in their as-prepared form and at various levels of photochemical reduction. With added electrons (arrow), faster inversion recovery is observed. For the same reduction levels, the spin−spin relaxation times (T_2) were also measured by monitoring the Hahn echo intensity as a function of delay time ($\pi/2 - \tau - \pi - \tau$ − echo). These curves are plotted in Figure 2c. T_2 also becomes shorter with added electrons. With increased photochemical reduction, both the spin−lattice and spin−spin relaxation rates are thus accelerated. To estimate T_1 and T_2 from these measurements, the spectra in Figure 2b,c were fit to eqs 1a and 1b, respectively. Neither data set follows purely single-exponential decay, but for the purposes of this study, an effective single-exponential time is most useful for quantifying the changes in relaxation dynamics.

$$I(\tau) = 1 - A_1 \exp\left(-\frac{\tau}{T_1}\right) \quad (1a)$$

$$I(2\tau) = A_2 \exp\left(-\frac{2\tau}{T_2}\right) \quad (1b)$$

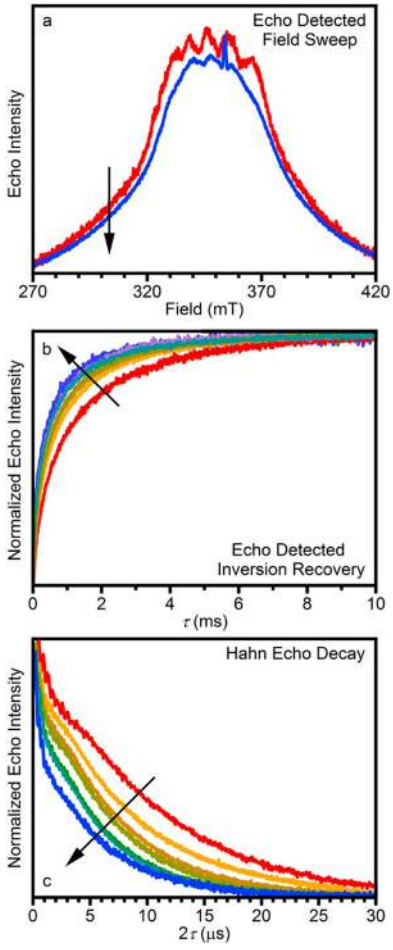

Figure 2. (a) Echo-detected field-sweep measurements of as-prepared (red) and fully reduced (blue) d = 3.7 nm $Zn_{0.9997}Mn_{0.0003}O$ nanocrystals. (b,c) Measurements of T_1 and T_2, respectively, for the same nanocrystals at various levels of photochemical reduction. Arrows indicate increased photochemical reduction. All measurements were performed at 4.5 K.

The effect of added electrons is most easily visualized by plotting the relaxation times as a function of the number of conduction band electrons per nanocrystal. Figure 3a and b plots T_1 and T_2, respectively, as a function of the average number of electrons per nanocrystal (top axes) and of the average electron density (bottom axes) for the 3.7 nm $Zn_{0.9997}Mn_{0.0003}O$ nanocrystals. The solid lines are guides to the eye. From these data, the addition of one electron per nanocrystal leads to a rapid decrease of both the spin−lattice and spin−spin relaxation times, causing both T_1 and T_2 to drop to around half of their initial values. The same experiments were performed on d = 3.7 nm $Zn_{0.996}Mn_{0.004}O$ nanocrystals, and the results are plotted in Figure 3c,d. Again, a rapid decrease in T_1 occurs upon the addition of one electron. A similar trend is not observed for T_2 in this sample, possibly because T_2 is already dominated by Mn^{2+}−Mn^{2+} interactions at this higher Mn^{2+} concentration.

The increased intensity of the Mn^{2+} CW EPR spectrum (Figure 1) upon photochemical reduction has been shown to arise from electron-mediated exchange interactions between Mn^{2+} dopants.[14] Excess electrons allow Mn^{2+} ions to overcome antiferromagnetic nearest-neighbor exchange interactions, increasing the CW EPR intensity.[14] In contrast with this

DOI: 10.1021/acs.jpclett.5b00621
J. Phys. Chem. Lett. 2015, 6, 1748−1753

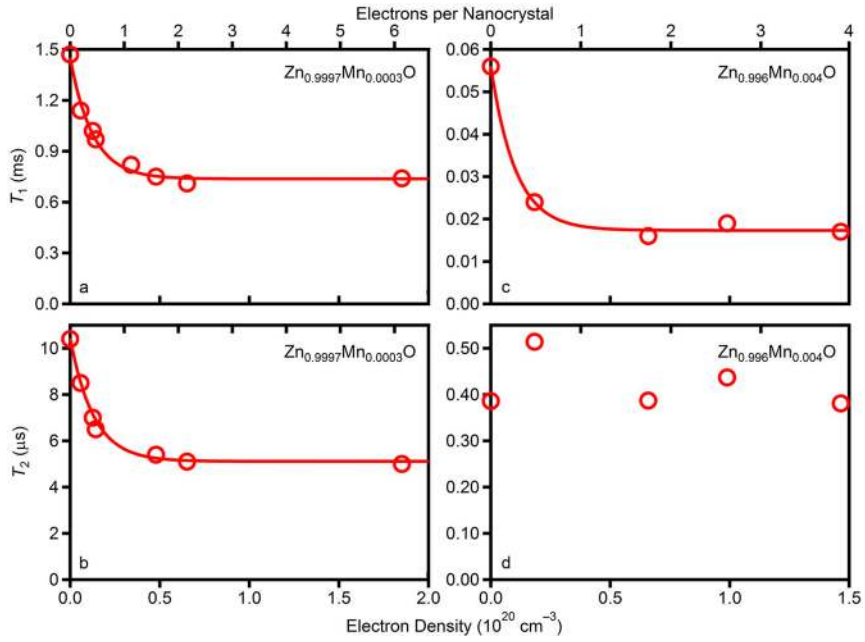

Figure 3. Change in T_1 and T_2 with increased photochemical reduction for (a,b) d = 3.7 nm $Zn_{0.9997}Mn_{0.0003}O$ and (c,d) d = 3.7 nm $Zn_{0.996}Mn_{0.004}O$ nanocrystals. The level of added electrons is given in terms of both electron density (bottom axes) and electrons per nanocrystal (top axes). The solid curves are guides to the eye. All measurements were performed at 4.5 K.

Scheme 1

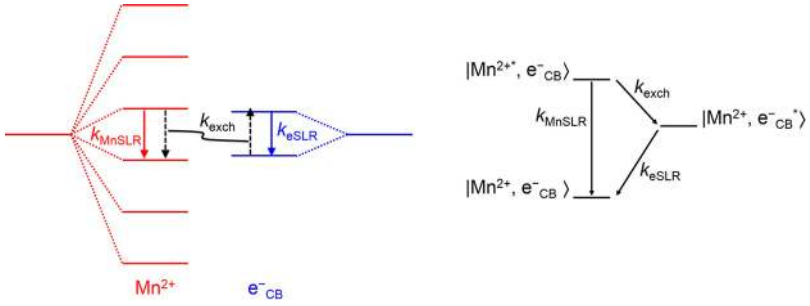

intensity increase, the ESE intensity decreases upon addition of electrons (Figure 2a). This decrease is due to fast spin relaxation, leading to reduced intensity at the time of the first data point in the spin-echo measurement. For the reduced nanocrystals, the faster spin relaxation means greater dephasing before the spins are refocused, leading to a smaller echo intensity. Broadening is more pronounced in the CW spectrum than in the ESE spectrum, suggesting that some of this broadening is inhomogeneous and thus can be overcome by employing an echo sequence.

To first order, an isolated Mn^{2+} ion has zero orbital moment in its ground state and thus cannot transfer energy efficiently to the lattice via spin−orbit and orbit−lattice interactions, giving it a relatively long T_1. Therefore, the largest contribution to Mn^{2+} spin−lattice relaxation is due to interactions between adjacent Mn^{2+} ions, making T_1 highly dependent on Mn^{2+} concentration.[21] This Mn^{2+} concentration dependence is observed in the spin−lattice relaxation times of these $Zn_{1-x}Mn_xO$ nanocrystals; T_1 is shorter at higher Mn^{2+} concentrations (Figure 3a,c). A similarly strong concentration dependence is also observed for T_2 (Figure 3b,d). At relatively low Mn^{2+} concentrations, such as the ones in this study, spin−spin interactions are dominated by the magnetic dipole−dipole interaction.[21] This mechanism is inversely dependent on interdipole distance, consistent with smaller T_2 values for higher Mn^{2+} concentrations. A strong dependence of T_1 and T_2 on Mn^{2+} concentration has been observed in a variety of bulk Mn^{2+}-doped II−VI semiconductors.[22−25]

Spin−orbit coupling is stronger for the conduction band electron than for Mn^{2+}. Energy transfer between conduction band electron spins and the lattice is therefore more efficient, and the electron's spin−lattice relaxation is much faster. In the n-type $Zn_{1-x}Mn_xO$ nanocrystals, these electron spins are also coupled to Mn^{2+} spins, which opens alternative channels for Mn^{2+} spin−lattice relaxation via exchange scattering.[21] Such effects have been observed in (Cd,Mn)Te and (Zn,Mn)Se quantum wells, where Mn^{2+} spin−lattice relaxation is controlled by excess electrons or holes.[26] This new relaxation pathway is depicted in Scheme 1(left).

Mn^{2+} spin relaxation via electron spin−lattice relaxation relies on efficient exchange scattering. This interaction must conserve energy as well as spin. The Zeeman splitting of the conduction band electron spin ($\Delta E_e = g_e\mu_B H$, where g_e is the electron g value, μ_B is the Bohr magneton, and H is the applied magnetic field) is slightly smaller than that of the Mn^{2+} spins ($\Delta E_{Mn} = g_{Mn}\mu_B H$), owing to its smaller g value ($g_e \approx 1.96$ and $g_{Mn} \approx 2.00$). The similar Zeeman splittings of the two subsystems and the exchange interactions between them enable

DOI: 10.1021/acs.jpclett.5b00621
J. Phys. Chem. Lett. 2015, 6, 1748−1753

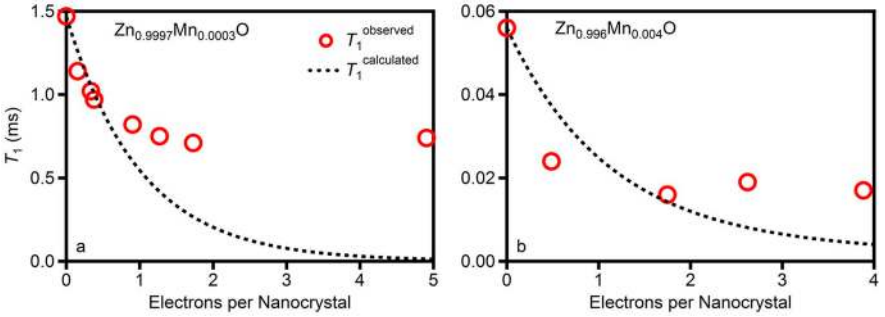

Figure 4. Experimental (circles) and calculated (dashed line) T_1 values plotted versus the average number of conduction band electrons for (a) d = 3.7 nm $Zn_{0.9997}Mn_{0.0003}O$ and (b) d = 3.7 nm $Zn_{0.996}Mn_{0.004}O$ nanocrystals. Calculated values were obtained using eq 2 with $T_1^{Mn} = T_1^{as\text{-}prepared}$ and T_1^{e} = 10 μs. All measurements were performed at 4.5 K.

very efficient energy transfer even at low temperatures. Fast electron spin−lattice relaxation in conjunction with strong electron−Mn^{2+} exchange thus accelerates the Mn^{2+} spin relaxation.

Scheme 1(right) illustrates the aforementioned process kinetically. Here, $k_{exch} = 1/T_{exch}$ describes the Mn^{2+} exchange scattering, which is generally very fast (10^{-12}−10^{-11} s)[27−29] and allows the Mn^{2+} excited spin state ($|Mn^{2+}*, e_{CB}^-\rangle$) and the electron excited spin state ($|Mn^{2+}, e_{CB}^-*\rangle$) to reach thermal equilibrium. The ground state can then be recovered via (i) direct coupling of Mn^{2+} spins with lattice phonons ($k_{MnSLR} = 1/T_1^{as\text{-}prepared}$) as in the absence of excess electrons or (ii) coupling of electron spins with lattice phonons ($k_{eSLR} = 1/T_1^{e}$).

In this kinetic model, recovery of the ground-state population is described by eq 2, where n_e is the integer number of conduction band electrons in a given nanocrystal and $\langle n\rangle$ is the ensemble average number of conduction band electrons per nanocrystal. A Poissonian distribution (eq 2b) is used to approximate the combined effects of discrete electron occupancies and inhomogeneously broadened redox and charging potentials.

$$T_1^{observed} = \sum_{n_e=0}^{10} \frac{P(n_e)}{k_{MnSLR} + n_e k_{eSLR}} = \sum_{n_e=0}^{10} \frac{P(n_e)}{1/T_1^{Mn} + n_e/T_1^{e}} \quad (2a)$$

$$P(n_e) = \frac{\langle n\rangle^{n_e} e^{-\langle n\rangle}}{n_e!} \quad (2b)$$

Figure 4 compares experimental T_1 values with those calculated from eq 2 using $T_1^{Mn} = T_1^{as\text{-}prepared}$ and T_1^{e} = 10 μs (Figure S2, Supporting Information). For simplicity, the same T_1^{e} was used for all nanocrystal reduction levels (see below). This simple model successfully reproduces the main qualitative experimental trends in Figure 4 well, and its quantitative inaccuracies are revealing. Specifically, the experimental data reach a minimum $T_1^{observed}$ value at an average of approximately one electron per nanocrystal and then level off at this value, whereas the model predicts continued decrease of T_1 with further addition of electrons. Phenomenologically, the electron spin density experienced by Mn^{2+} no longer increases after this point. The approximation of a constant T_1^{e} cannot be the source of this disagreement between model and experiment because T_1^{e} likely decreases with increasing $\langle n\rangle$, but the model already overestimates the decrease in T_1^{Mn} at $\langle n\rangle > 1$. Instead, this difference between model and experiment suggests that electron−electron spin-pairing interactions in multiply reduced nanocrystals yield low- or intermediate-spin configurations with spin densities that do not scale in simple proportion to the number of electrons. Pairing of conduction band electron spins is not accounted for in the model, which implicitly assumes noninteracting electrons. In bulk DMSs, this is equivalent to saying that only electrons at or near the Fermi level can participate in Mn^{2+} spin flips because deeper electrons will not gain sufficient energy from Mn^{2+} to reach unoccupied final states, and the number of possible electron spin flips (and hence also the electron-mediated spin−lattice relaxation rate) plateaus when the Fermi level is raised sufficiently.[18] This reasoning has been used to explain a similar dependence of Mn^{2+} spin−lattice relaxation times on free-electron concentrations in $Zn_{0.996}Mn_{0.004}Se$/$Zn_{0.94}Be_{0.06}Se$ quantum wells.[21,22] Indeed, accounting for spin-pairing effects explicitly under an assumption of atom-like filling of conduction band S, P, and D levels causes the model to predict larger values of $T_1^{observed}$ at large $\langle n\rangle$ (Figure S3, Supporting Information). Further refinement of the model to better reproduce the data would require assumptions that are not warranted by the data; therefore, only results from the simplest model are displayed in Figure 4.

To illustrate the role of electron density, parallel measurements were performed on larger (d = 7.8 nm) $Zn_{0.997}Mn_{0.003}O$ nanocrystals. These data are summarized in Figure 5, which plots normalized T_1 times as a function of electron density for each sample of $Zn_{1-x}Mn_xO$ nanocrystals. For the larger nanocrystals, much smaller maximum electron densities were

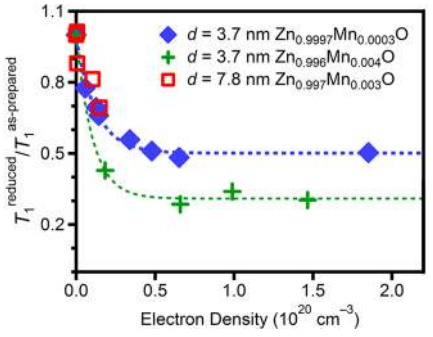

Figure 5. Normalized Mn^{2+} spin−lattice relaxation in reduced nanocrystals ($T_1^{reduced}/T_1^{as\text{-}prepared}$) as a function of carrier density for d = 3.7 nm $Mn_{0.0003}Zn_{0.9997}O$ (blue diamonds), d = 3.7 nm $Mn_{0.004}Zn_{0.996}O$ (green plus signs), and d = 7.8 nm $Mn_{0.003}Zn_{0.997}O$ (red squares) nanocrystals. The dashed curves are guides to the eye. All measurements were performed at 4.5 K.

DOI: 10.1021/acs.jpclett.5b00621
J. Phys. Chem. Lett. 2015, 6, 1748−1753

achieved, possibly due to competitive hole trapping by Mn^{2+} during photodoping. A similar trend of decreasing T_1 with increasing electron density is observed for all samples, but for the d = 7.8 nm nanocrystals, T_1 is still decreasing after the addition of ~4 conduction band electrons. This result confirms that the trends in T_1 in these nanocrystals are determined by electron density rather than electron count. Overall, the observation that T_1 becomes insensitive to electron density beyond $\sim 5 \times 10^{-19}$ cm^{-3} thus suggests that, at these high electron densities, the carrier spin density experienced by Mn^{2+} becomes independent of the total electron density.

The impressive magneto-optical effects observed in DMSs, such as giant Zeeman splittings, result from strong exchange interactions between charge carriers and magnetic dopants.[30] The results presented here illustrate that DMS spin dynamics can also be controlled using such exchange interactions, via spin and energy transfer between the magnetic dopants, charge carriers, and lattice excitations (e.g., phonons).[21] Colloidal $Zn_{1-x}Mn_xO$ nanocrystals are attractive model systems for probing these spin dynamics in DMS nanostructures. The pulsed EPR data presented here demonstrate large changes in Mn^{2+} spin dynamics upon introduction of small numbers of excess conduction band electrons into colloidal $Zn_{1-x}Mn_xO$ nanocrystals, arising from the introduction of new Mn^{2+}–carrier exchange coupling pathways. The experimental observations are understood in terms of Mn^{2+} spin transfer to the conduction band electrons, and a simple model is described that reproduces the main experimental observations. These results illustrate the capability to use nanocrystal charge-state control for tuning dopant spin dynamics relevant to future spintronic applications of this class of materials.

METHODS

Nanocrystal Synthesis. Colloidal d = 3.7 nm $Zn_{1-x}Mn_xO$ nanocrystals were synthesized by base hydrolysis as described previously.[16] First, 13 mmol of zinc acetate dihydrate was dissolved in 135 mL of dimethyl sulfoxide at room temperature. Once the zinc precursor was fully dissolved, 1–15 μmol of manganese acetate dihydrate was added. This solution was stirred while a solution of 22 mmol of tetramethylammonium hydroxide pentahydrate in 40 mL of ethanol was added dropwise. Nanocrystals were grown for 30 min, after which the reaction was stopped by precipitation with ~300 mL of ethyl acetate. Nanocrystals were collected via centrifugation followed by resuspension in ethanol and precipitation with heptane. In order to make the nanocrystals soluble in nonpolar solvents, a ligand exchange was done by suspending nanocrystals in ethanol and precipitating them with an excess of dodecylamine (DDA) that had been heated above 29 °C. Finally, the nanocrystals were surface treated by heating in 90% trioctylphosphine oxide (TOPO) at ~100 °C for 30 min. The nanocrystals were then washed/resuspended with EtOH/toluene as described above. Large Mn^{2+}-doped ZnO nanocrystals were synthesized following the above procedure but were grown for 24 h before precipitation with ethyl acetate. Additionally, before treatment with TOPO, nanocrystals were heated under N_2 in DDA at 180 °C for 20 min followed by precipitation with ethanol and collection by centrifugation.

Physical Characterization. The Mn^{2+} mole fraction (x) was determined by inductively coupled plasma atomic emission spectroscopy. CW EPR spectra (295 K) were performed using a Bruker EMX X-band spectrometer with a Bruker SHQE resonator operating at a microwave frequency of 9.8 GHz.

Photochemical Reduction. UV illumination under anaerobic conditions generates holes that may be quenched by ethanol or other hole acceptors, leaving behind kinetically stable conduction band electrons (e^-_{CB}).[11,13,14] Continued illumination allows accumulation of multiple e^-_{CB} per nanocrystal, which can be monitored by the appearance and growth of an absorption band in the IR and a bleach of the band-edge absorption. Nanocrystals are referred to as fully reduced when continued photoexcitation no longer alters the intensity or position of the IR absorption peak. Anaerobic $Zn_{1-x}Mn_xO$ nanocrystal solutions were prepared in EPR tubes in an inert-atmosphere glovebox. The tubes were then sealed under vacuum to maintain the inert environment. These samples were photochemically reduced via irradiation with a 100 W Hg/Xe Oriel photolysis lamp (~2 W/cm^2, ~1.5 cm illumination diameter) using aqueous $CuSO_4$ to filter out IR photons. Electron densities were determined via titration against $[FeCp^*_2][BAr_F]$ ($[FeCp^*_2]^+$ = decamethylferrocenium, $[BAr_F]^-$ = tetrakis[3,5-bis(trifluoromethyl)phenyl]borate).[13]

Pulsed EPR Spectroscopy. Pulsed EPR experiments (4.5 K) were performed on a Bruker E580 X-band spectrometer with an ER 4118 X-MD5 resonator operating at a microwave frequency of 9.7 GHz. The sample and probe were mounted inside of an Oxford Instruments CF935O dynamic continuous flow cryostat. The temperature was controlled and monitored with an Oxford Instrument ITC5035 temperature controller and a Cernox Resistor CX-1050-AA-1.4L temperature sensor (LakeShore). ESE spectra were obtained by measuring the standing Hahn echo intensity ($\pi/2 - T_{fixed} - \pi - T_{fixed}$ – echo) as a function of transverse field. The delay time (T_{fixed}) was 124 ns between the tipping ($\pi/2$) and refocusing (π) pulses. T_1 was measured using an echo-detected inversion recovery pulse sequence ($\pi - \tau - \pi/2 - T_{fixed} - \pi - T_{fixed}$ – echo). T_2 was measured using a standard two-pulse Hahn echo sequence ($\pi/2 - \tau - \pi - \tau$ – echo). The length of the $\pi/2$ (π) pulse for all experiments was 16 ns (32 ns).

ASSOCIATED CONTENT

Supporting Information

CW EPR spectra of $Zn_{0.9997}Mn_{0.0003}O$ nanocrystals and inversion recovery data for reduced ZnO nanocrystals. The Supporting Information is available free of charge on the ACS Publications website at DOI: 10.1021/acs.jpclett.5b00621.

AUTHOR INFORMATION

Corresponding Author

*E-mail: Gamelin@chem.washington.edu.

Present Addresses

†J.D.R.: Department of Chemistry and Biochemistry, University of California in San Diego, La Jolla, CA 92093, U.S.A.

‡S.T.O.: Laboratory for Neutron Scattering and Imaging, Paul Scherrer Institute, CH-5232 Villigen PSI, Switzerland.

Notes

The authors declare no competing financial interest.

ACKNOWLEDGMENTS

Support from the U.S. National Science Foundation (DMR-1206221 to D.R.G. and Graduate Research Fellowship DGE-1256082 to A.M.S.) is gratefully acknowledged. Additional funding was provided by a Department of Energy, Energy Efficiency and Renewable Energy (DOE-EERE) Fellowship to J.D.R.

DOI: 10.1021/acs.jpclett.5b00621
J. Phys. Chem. Lett. 2015, 6, 1748–1753

REFERENCES

(1) Wolf, S. A.; Awschalom, D. D.; Buhrman, R. A.; Daughton, J. M.; von Molnár, S.; Roukes, M. L.; Chtchelkanova, A. Y.; Treger, D. M. Spintronics: A Spin-Based Electronics Vision for the Future. *Science* **2001**, *294*, 1488−1495.

(2) Zutic, I.; Fabian, J.; Das Sarma, S. Spintronics: Fundamentals and Applications. *Rev. Mod. Phys.* **2004**, *76*, 323−410.

(3) Hanson, R.; Kouwenhoven, L. P.; Petta, J. R.; Tarucha, S.; Vandersypen, L. M. K. Spins in Few-Electron Quantum Dots. *Rev. Mod. Phys.* **2007**, *79*, 1217.

(4) Kobak, J.; Smoleński, T.; Goryca, M.; Papaj, M.; Gietka, K.; Bogucki, A.; Koperski, M.; Rousset, J. G.; Suffczyński, J.; Janik, E.; Nawrocki, M.; Golnik, A.; Kossacki, P.; Pacuski, W. Designing Quantum Dots for Solotronics. *Nat. Commun.* **2014**, *5*, 3191.

(5) Jonker, B. T.; Park, Y. D.; Bennett, B. R.; Cheong, H. D.; Kioseoglou, G.; Petrou, A. Robust Electrical Spin Injection into a Semiconductor Heterostructure. *Phys. Rev. B* **2000**, *62*, 8180−8183.

(6) Ohno, Y.; Young, D. K.; Beschoten, B.; Matsukura, F.; Ohno, H.; Awschalom, O. O. Electrical Spin Injection in a Ferromagnetic Semiconductor Heterostructure. *Nature* **1999**, *402*, 790−792.

(7) Ruster, C.; Borzenko, T.; Gould, C.; Schmidt, G.; Molenkamp, L. W.; Liu, X.; Wojtowicz, T. J.; Furdyna, J. K.; Yu, Z. G.; Flatte, M. E. Very Large Magnetoresistance in Lateral Ferromagnetic (Ga,Mn)As Wires with Nanoconstrictions. *Phys. Rev. Lett.* **2003**, *91*, 216602.

(8) Besombes, L.; Cao, C. L.; Jamet, S.; Boukari, H.; Fernández-Rossier, J. Optical Control of the Spin State of Two Mn Atoms in a Quantum Dot. *Phys. Rev. B* **2012**, *86*, 165306.

(9) Krebs, O.; Lemaître, A. Optically Induced Coupling of Two Magnetic Dopant Spins by a Photoexcited Hole in a Mn-Doped InAs/GaAs Quantum Dot. *Phys. Rev. Lett.* **2013**, *111*, 187401.

(10) Beaulac, R.; Ochsenbein, S. T.; Gamelin, D. R. In *Colloidal Transition-Metal-Doped Quantum Dots*; CRC Press: Boca Raton, FL, 2010; pp 397−453.

(11) Liu, W. K.; Whitaker, K. M.; Kittilstved, K. R.; Gamelin, D. R. Stable Photogenerated Carriers in Magnetic Semiconductor Nanocrystals. *J. Am. Chem. Soc.* **2006**, *128*, 3910−3911.

(12) Rinehart, J. D.; Schimpf, A. M.; Weaver, A. L.; Cohn, A. W.; Gamelin, D. R. Photochemical Electronic Doping of Colloidal CdSe Nanocrystals. *J. Am. Chem. Soc.* **2013**, *135*, 18782−18785.

(13) Schimpf, A. M.; Gunthardt, C. E.; Rinehart, J. D.; Mayer, J. M.; Gamelin, D. R. Controlling Carrier Densities in Photochemically Reduced Colloidal ZnO Nanocrystals: Size Dependence and Role of the Hole Quencher. *J. Am. Chem. Soc.* **2013**, *135*, 16569−16577.

(14) Ochsenbein, S. T.; Feng, Y.; Whitaker, K. M.; Badaeva, E.; Liu, W. K.; Li, X.; Gamelin, D. R. Charge-Controlled Magnetism in Colloidal Doped Semiconductor Nanocrystals. *Nat. Nanotechnol.* **2009**, *4*, 681−687.

(15) Beaulac, R.; Schneider, L.; Archer, P. I.; Bacher, G.; Gamelin, D. R. Light-Induced Spontaneous Magnetization in Colloidal Doped Quantum Dots. *Science* **2009**, *325*, 973−976.

(16) Norberg, N. S.; Kittilstved, K. R.; Amonette, J. E.; Kukkadapu, R. K.; Schwartz, D. A.; Gamelin, D. R. Synthesis of Colloidal Mn^{2+}:ZnO Quantum Dots and High-T_C Ferromagnetic Nanocrystalline Thin Films. *J. Am. Chem. Soc.* **2004**, *126*, 9387−9398.

(17) Liu, W. K.; Whitaker, K. M.; Smith, A. L.; Kittilstved, K. R.; Robinson, B. H.; Gamelin, D. R. Room-Temperature Electron Spin Dynamics in Free-Standing ZnO Quantum Dots. *Phys. Rev. Lett.* **2007**, *98*, 186804.

(18) Cohn, A. W.; Janßen, N.; Mayer, J. M.; Gamelin, D. R. Photocharging ZnO Nanocrystals: Picosecond Hole Capture, Electron Accumulation, and Auger Recombination. *J. Phys. Chem. C* **2012**, *116*, 20633−20642.

(19) Whitaker, K. M.; Ochsenbein, S. T.; Polinger, V. Z.; Gamelin, D. R. Electron Confinement Effects in the EPR Spectra of Colloidal n-Type ZnO Quantum Dots. *J. Phys. Chem. C* **2008**, *112*, 14331−14335.

(20) Schimpf, A. M.; Thakkar, N.; Gunthardt, C. E.; Masiello, D. J.; Gamelin, D. R. Charge-Tunable Quantum Plasmons in Colloidal Semiconductor Nanocrystals. *ACS Nano* **2014**, *8*, 1065−1072.

(21) Yakovlev, D. R.; Merkulov, I. A., Spin and Energy Transfer between Carriers, Magnetic Ions and Lattice. In *Introduction to the Physics of Diluted Magnetic Semiconductors*; Gaj, J. A., Kossut, J., Eds.; Springer: New York, 2011; Vol. *144*.

(22) Kneip, M. K.; Yakovlev, D. R.; Bayer, M.; Maksimov, A. A.; Tartakovskii, I. I.; Keller, D.; Ossau, W.; Molenkamp, L. W.; Waag, A. Spin−Lattice Relaxation of Mn Ions in ZnMnSe/ZnBeSe Quantum Wells Measured under Pulsed Photoexcitation. *Phys. Rev. B* **2006**, *73*, 045305.

(23) Dietl, T.; Peyla, P.; Grieshaber, W.; Daubigne, Y. M. Dynamics of Spin Organization in Diluted Magnetic Semiconductors. *Phys. Rev. Lett.* **1995**, *74*, 474−477.

(24) Farah, W.; Scalbert, D.; Nawrocki, M. Magnetic Relaxation Studied by Transient Reflectivity in $Cd_{1-x}Mn_xTe$. *Phys. Rev. B* **1996**, *53*, R10461−R10464.

(25) Scherbakov, A. V.; Akimov, A. V.; Yakovlev, D. R.; Ossau, W.; Landwehr, G.; Wojtowicz, T.; Karczewski, G.; Kossut, J. Spin−Lattice Relaxation in Semimagnetic CdMnTe/CdMgTe Quantum Wells. *Phys. Rev. B* **2000**, *62*, R10641−R10644.

(26) Scherbakov, A.; Yakovlev, D.; Akimov, A.; Merkulov, I.; König, B.; Ossau, W.; Molenkamp, L.; Wojtowicz, T.; Karczewski, G.; Cywinski, G. Acceleration of the Spin−Lattice Relaxation in Diluted Magnetic Quantum Wells in the Presence of a Two-Dimensional Electron Gas. *Phys. Rev. B* **2001**, *64*, 155205.

(27) Akimov, A. V.; Scherbakov, A. V.; Yakovlev, D. R.; Merkulov, I. A.; Bayer, M.; Waag, A.; Molenkamp, L. W. Multiple Transfer of Angular Momentum Quanta from a Spin-Polarized Hole to Magnetic Ions in $Zn_{1-x}Mn_xSe/Zn_{1-y}Be_ySe$ Quantum Wells. *Phys. Rev. B* **2006**, *73*, 165328.

(28) Kneip, M. K.; Yakovlev, D. R.; Bayer, M.; Maksimov, A. A.; Tartakovskii, I. I.; Keller, D.; Ossau, W.; Molenkamp, L. W.; Waag, A. Direct Energy Transfer from Photocarriers to Mn-Ion System in II−VI Diluted-Magnetic-Semiconductor Quantum Wells. *Phys. Rev. B* **2006**, *73*, 035306.

(29) Baumberg, J. J.; Crooker, S. A.; Awschalom, D. D.; Samarth, N.; Luo, H.; Furdyna, J. K. Ultrafast Faraday Spectroscopy in Magnetic Semiconductor Quantum Structures. *Phys. Rev. B* **1994**, *50*, 7689−7700.

(30) Furdyna, J. K., Kossut, J., Eds. Diluted Magnetic Semiconductors. *Semiconductors and Semimetals*; Academic: New York, 1988; Vol. *25*.

DOI: 10.1021/acs.jpclett.5b00621
J. Phys. Chem. Lett. 2015, 6, 1748−1753